Title
Methods for Analysis of Regeneration in Fibrotic Muscle

Author
Nakaki, Matthew John

Publication Date
2021

Peer reviewed|Thesis/dissertation

Methods for Analysis of Regeneration in Fibrotic Muscle

By

MATTHEW NAKAKI
THESIS

Submitted in partial satisfaction of the requirements for the degree of

MASTER OF SCIENCE

in

Biomedical Engineering

in the

OFFICE OF GRADUATE STUDIES

of the

UNIVERSITY OF CALIFORNIA

DAVIS

Approved:

Lucas Smith, Chair

Scott Simon

Erkin Seker

Committee in Charge

2021

Abstract

Morphology of the skeletal muscle is highly indicative of its function and health. In diseases like Duchenne muscular dystrophy (DMD), fibrosis develops within the muscles and the morphology of the muscle changes considerably. Histology is the gold standard for assessing the morphology of the muscles in both research and clinical settings. Whole muscles can be composed of thousands of fibers in parallel making quantification of parameters like number and size of muscle fibers difficult by manual methods. We present SMASH 2.0 as a tool for automated analysis of histological muscle images that makes use of machine learning algorithms. The classifier trained to distinguish muscle fibers in the images was able to identify muscle fibers with 99.5% sensitivity and 98.4% specificity. The data output by SMASH was not found to be significantly different from manual analysis.

Skeletal muscle is also a heterogeneous tissue containing many types of cells in addition to muscle cells. Among these are satellite cells, a population of stem cells that reside at the periphery of muscle fibers and are the primary mediators of the muscle's regenerative capabilities. Satellite cells that migrate through fibrotic tissue have been shown to have DNA damage and impaired differentiation. Methods of imaging satellite cell migration through constrictions are limited. We present two microfluidic devices, one with pores of a defined size and one that accommodates tunable collagen matrices, which are optimized for real time imaging of myoblast migration through small constrictions.

These tools will help elucidate the link between constricted migration and impaired regeneration seen in DMD and can provide a method for assessing the efficacy of therapeutic treatments for muscle fibrosis.

Chapter 1. Background

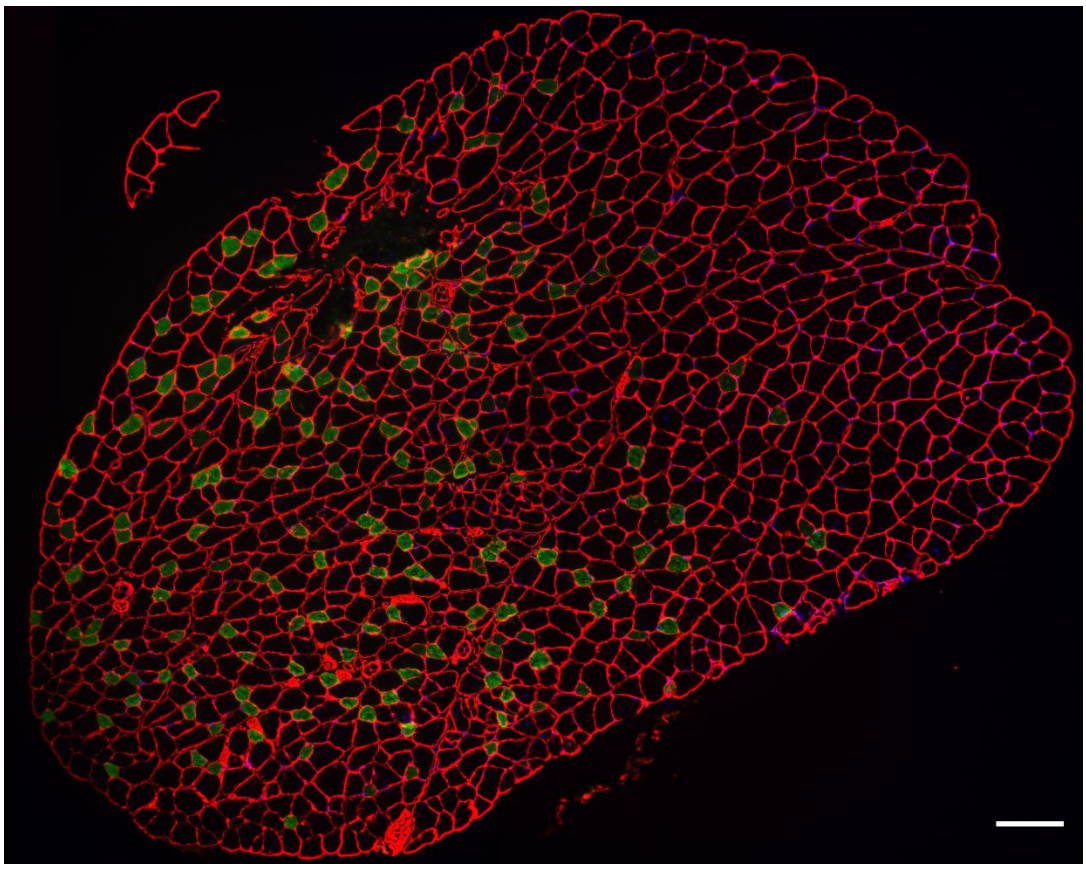

Figure 1. Representative immunofluorescent image of a mouse extensor digitorum longus muscle cross section. Red shows muscle fiber outlines; Green show myosin heavy chain IIa; Blue shows myonuclei. Scale bar 100 μm.

Skeletal muscle tissue is important for overall health and constitutes a large portion of a typical adult's body mass. Skeletal muscles are primarily composed of contractile, multinucleated muscle fibers where morphology is closely linked to the function and health of the muscle. The number and cross-sectional area of the fibers are indicative of the number of sarcomeres in parallel and the contractile properties of the fibers. Skeletal muscle is a highly adaptable tissue and is capable of robust regeneration following damage. Regeneration of the muscle fibers is apparent as a shift of myonuclei from the periphery of the fibers toward the center [1]. Fibrosis also becomes evident as a buildup of extracellular matrix (ECM) within the muscle's interstitial space [2]. These metrics are routinely assessed using histology. Histochemical stains such as

hematoxylin and eosin and Masson's trichrome are common for analyzing the overall morphology of the muscle. Sirius red stain is used to selectively stain collagen, the main component of the muscle extracellular matrix. Immunofluorescent techniques can also be used to label specific structures within the muscle. Antibodies against laminin or dystrophin can be used to visualize the borders of muscle fibers and antibodies against specific myosin heavy chain isoforms can be used to identify muscle fiber type [3]. Muscle fiber type is defined by the myosin ATPase activity of the fiber and can be broadly classified as type I slow fibers or type II fast fibers.

Duchenne muscular dystrophy (DMD) is a notable example of a disease state where both the function and morphology of the muscles change dramatically. As the disease progresses, contractile muscle tissue is lost and replaced with fibrotic ECM and fat tissue [4]. Muscle fibers in DMD undergo continual cycles of damage and regeneration due to a mutation in the dystrophin gene. Dystrophin is a component of a protein complex that links the actin cytoskeleton of the muscle fibers to the extracellular matrix. The absence of dystrophin destabilizes plasma membrane of the muscle fiber leading to increased oxidative stress and damage to the fiber. These fibers also have predominantly centrally located nuclei which are a marker for regeneration. These morphological changes are easily visualized but are difficult to quantify and would benefit from automated histological analysis.

Muscles of DMD patients also have an impaired ability to regenerate efficiently. This regeneration is mediated by a population of muscle stem cells termed satellite cells. These cells become activated following myofiber damage then proliferate and migrate toward the site of damage to differentiate into mature muscle fibers [5]. Recent evidence suggests that satellite cell migration through fibrotic ECM imparts damage to the cells that impairs differentiation and

muscle repair. Current methods of imaging myoblasts as they migrate through small constrictions are limited as they do not allow the visualization of the entire process. Microfluidic devices have the capability to overcome these limitations and allow for precise control over the cell migration microenvironment.

In this thesis, we present three tools to improve the investigation of muscle pathologies, one software tool for assessing muscle morphology *in vivo* and two microfluidic devices for real-time observation of myoblast migration.

Chapter 2. SMASH 2.0: Machine Learning-Based Muscle Histology Analysis

Introduction

Histology is an important tool for qualitatively assessing the morphology of skeletal muscle as well as for quantifying various measures of muscle health. One of the most used metrics is the cross-sectional area of muscle fibers which can be an indicator of the muscle response to external stimuli. Muscle fiber hypertrophy can occur as a result of resistance training [6] and muscle fiber atrophy can occur from factors such as injury or disuse [7]. These measurements have traditionally been done by manually measuring muscle fiber outlines; however, this often makes analysis of muscle cross-sections time consuming and can introduce bias and variability between users.

Other metrics of interest include position of the myonuclei. Muscle fiber nuclei are typically found at the periphery of the muscle fibers while a nucleus near the center of the fiber is indicative of a regenerating fiber [1]. Muscle fiber type is also of interest as the distribution of muscle fiber type and the size of different muscle fiber types can change considerably in response to nerve activity, mechanical loading, and hormones [8]. Myosin heavy chain isoforms

are usually used as a marker for muscle fiber type and are easily visualized with immunostaining but are difficult to classify manually [3].

Several software tools have been introduced recently [9,10,11] to automate this analysis, but these tools currently do not address all of these metrics and still require a significant amount of user input in order to achieve an optimal result. Some of these tools are also closed source and are not free to use [12]. We have previously introduced SMASH [13], a semi-automatic, MATLAB-based app for this purpose. The goal of this study is to improve the performance of SMASH by inclusion of machine learning classifiers and a more user-friendly interface.

Implementation

Code development

SMASH app code and GUI were written and designed with MATLAB r2020a App Designer, Image Processing, and Curve Fitting Toolboxes (Mathworks, MA, USA). Machine learning classifiers were trained using MATLAB r2020a Machine Learning Toolbox. Training and test datasets were generated using a modified version of a previously published edition of SMASH. 61,335 data points were allocated to the training dataset and a further 50,771 data points were withheld for the validation dataset. Each data point represents either a manually labelled muscle fiber or a nonfiber object following image segmentation.

Mice/staining

Images associated with previous studies on muscle histology were used to train and test the machine learning classifiers [14]. Briefly, soleus, extensor digitorum longus, and tibialis anterior muscles were dissected from wildtype C57Bl/6 mice or from *mdx* mice. The muscles were sectioned and immunostained for laminin and either myosin heavy chain I or IIb and counterstained with DAPI to label nuclei (Fig. 1).

Statistical Analysis

Statistical tests were performed using Graphpad Prism 9. A two-tailed, paired t-test or one-way ANOVA with Tukey's multiple comparisons test was used.

Image segmentation

Once an image is selected, the user is prompted to segment the image as described previously using watershed transform (Fig. 2A). Differences in image brightness and imperfections in staining necessitate the use of an h-minima transform to suppress local minima in the intensity profile. In the prior version of SMASH, the user must manually input a pixel depth, below which, minima will be suppressed. To automate this process, a machine learning regression model based on a Gaussian support vector machine was trained using 24 sample images with a manually chosen segmentation value. The predictor variables used by this model are the average pixel intensity of the whole image, the average intensity of pixels forming part of the fiber borders, and the average intensity of background pixels. From these predictors, the model can discern the differences between pixels that are part of the background and pixels that are part of the fiber outlines and predict a segmentation value. A comparison of manually chosen segmentation values and predicted values did not produce significantly different results (Fig. 3). Due to the subjective nature of the segmentation process, it is difficult to assess the accuracy of

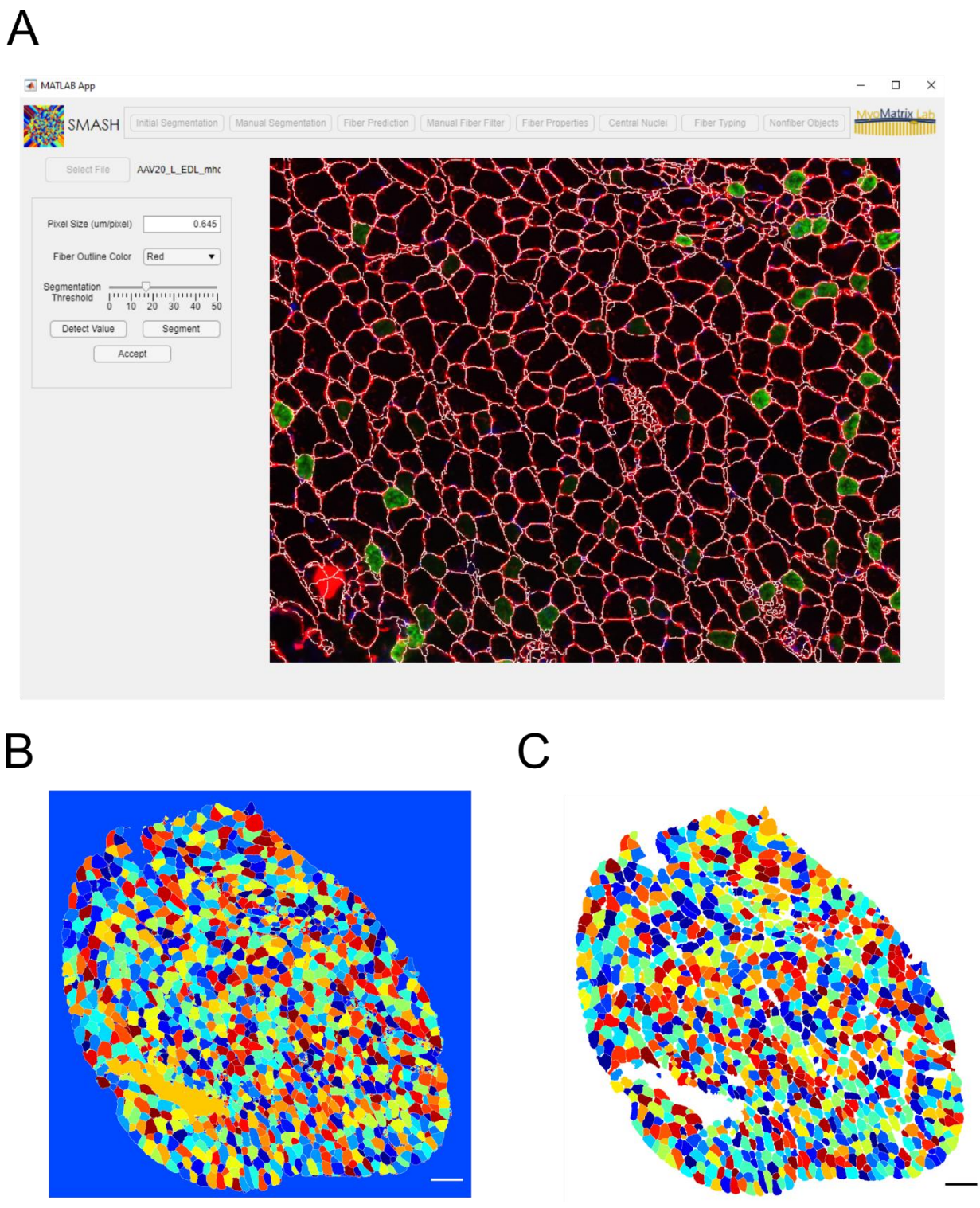

Figure 2. Functions of SMASH segmentation and output masks. (A) The SMASH user interface showing the segmentation function and the image to be segmented. Laminin stain is shown in red while white lines indicate detected fiber outlines based on watershed transform. (B) Mask containing segments following initial segmentation. Colors are randomly assigned to distinguish segments. (C) Final mask following filtering out of segments that do not represent muscle fibers. Scale bars 100 µm.

the model, but implementation of this model presents a significant improvement in the segmentation step as it eliminates the initial guess that is required in the previous edition of SMASH. If the user is not satisfied with the predicted segmentation value, they may quickly adjust the value at their discretion until the image is segmented adequately.

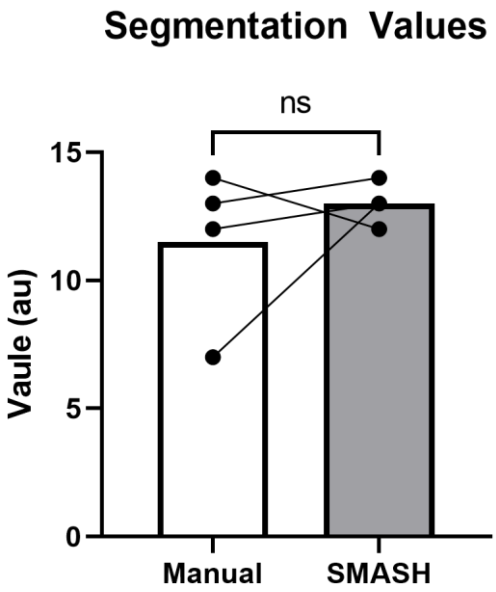

Figure 3. Comparison of manually chosen segmentation values and values predicted using the regression model. Values were not significantly different.

Muscle fiber prediction

Following image segmentation, segments representing muscle fibers must be filtered from segments that do not represent muscle fibers (Fig. 2B, C). To facilitate this step, several machine learning classifiers were trained using properties of 61,335 manually labelled image segments representing either muscle fibers or nonfiber objects. Of the classifiers trained, a medium decision tree classifier with 7 branch points was chosen as it resulted in a preliminary prediction accuracy of 99.5% as well as the fastest time to predict at 25 milliseconds which minimizes the need for powerful computer hardware and increases the accessibility of SMASH to a wide range of users. The kernel naïve Bayes classifier also produced a high true positive rate but had much

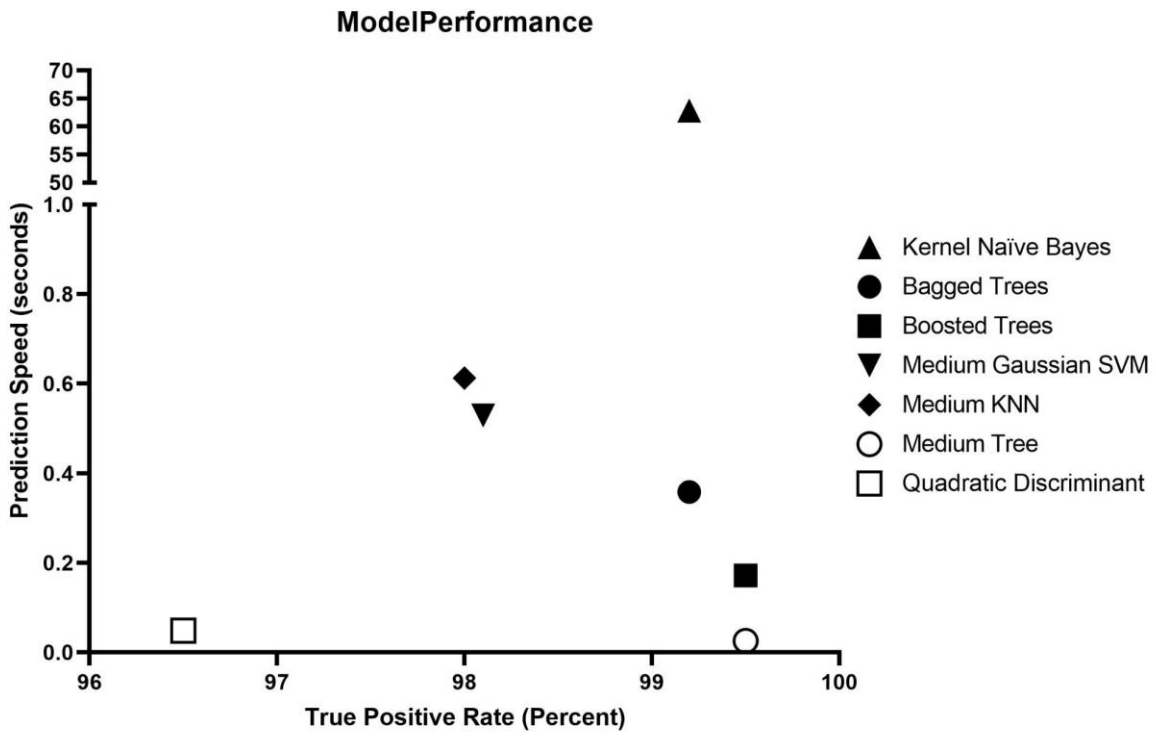

Figure 4. Classifier model performance measured by true positive predictive rate and time to make predictions on a test dataset.

slower prediction speed at 62 seconds to predict. Gaussian support vector machine and k-nearest neighbors classifiers produced lower true positive rates than any of the decision tree classifiers. Additionally, the ensemble methods of bagging and boosting decision trees did not improve the accuracy and slowed the time to predict (Fig. 4). The decision tree classifier's 7 branch points give the model sufficient specificity to accurately distinguish muscle fibers from nonfiber objects while avoiding overfitting to the training dataset (Fig. 6). Five predictor variables were selected for the model: cross sectional area, eccentricity, circularity, convexity, and extent of the segments. Eccentricity is calculated as the length between the center and one of the foci of an ellipse that approximates the segment divided by the length of its semi-major axis (Fig. 5B). Convexity is measured as the fraction of pixels within the segment that are also within the segment's convex hull (Fig. 5C). Similarly, extent is the fraction of pixels in the segment that are

also within the segment's bounding box (Fig. 5D). These predictors were chosen under the assumption that muscle fibers are generally found to be within a certain range of cross-sectional area. Muscle fibers also generally have a grossly circular appearance and have a high convexity. This is contrasted with interstitial spaces which contain many concavities from the presence of surrounding muscle fibers and often take on a stellate appearance.

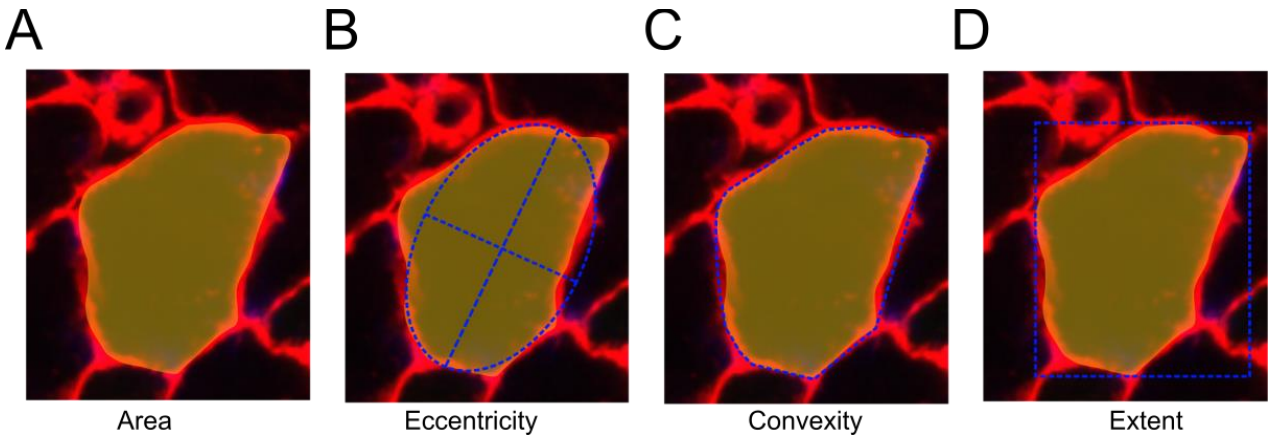

Figure 5. Illustration of the predictor variables used to classify the segments. (A) Cross sectional area of the segment shown in yellow. (B) Eccentricity of an ellipse approximating the segment shown in blue. (C) Convexity of the segment is represented as the fraction of pixels in the segment shown in yellow that are also within the segment's convex hull shown in blue. (D) Extent of the segment is shown as the fraction of the pixels in the segment shown in yellow that are also within the segment's bounding box shown in blue.

Results

Classifier validation

Following segmentation, a mask is generated containing all the segments and the five predictor variables are quantified for each segment formed in the image and passed to the classifier to predict if the segment represents a muscle fiber or a nonfiber object. Once a classification is assigned to each segment, a new mask is generated keeping only those segments that represent muscle fibers. To assess the performance of the classifier in its ability to accurately predict muscle fibers, data from a validation dataset containing 50,771 segments was fed into the classifier and the predicted class for each segment was compared to its known classification. The

classifier was found to have a true positive predictive value of 99.5% and a true negative predictive value of 98.4% (Fig. 7).

Once the segments are classified, a prediction score is also assigned to the segment representing the probability that the segment belongs to a certain class. The SMASH interface allows the user to specify a threshold value for the prediction score, in which each segment must exceed to be classified as a fiber. Each segment that has a prediction score below the threshold is sequentially presented to the user to be manually classified. In this way, the user is able to decide the degree to which they would like to automate the analysis or manually filter the segments. The original image as well as a color-coded mask is presented to the user to aid in this process. The mask colors segments cyan when the segment was predicted to be a fiber but has a prediction score below the specified threshold. Segments are colored magenta when they were predicted to be nonfiber objects and had a prediction score below the threshold. Green and red segments are those that were predicted to be fibers and nonfibers, respectively, and have a prediction score above the threshold (Fig. 8).

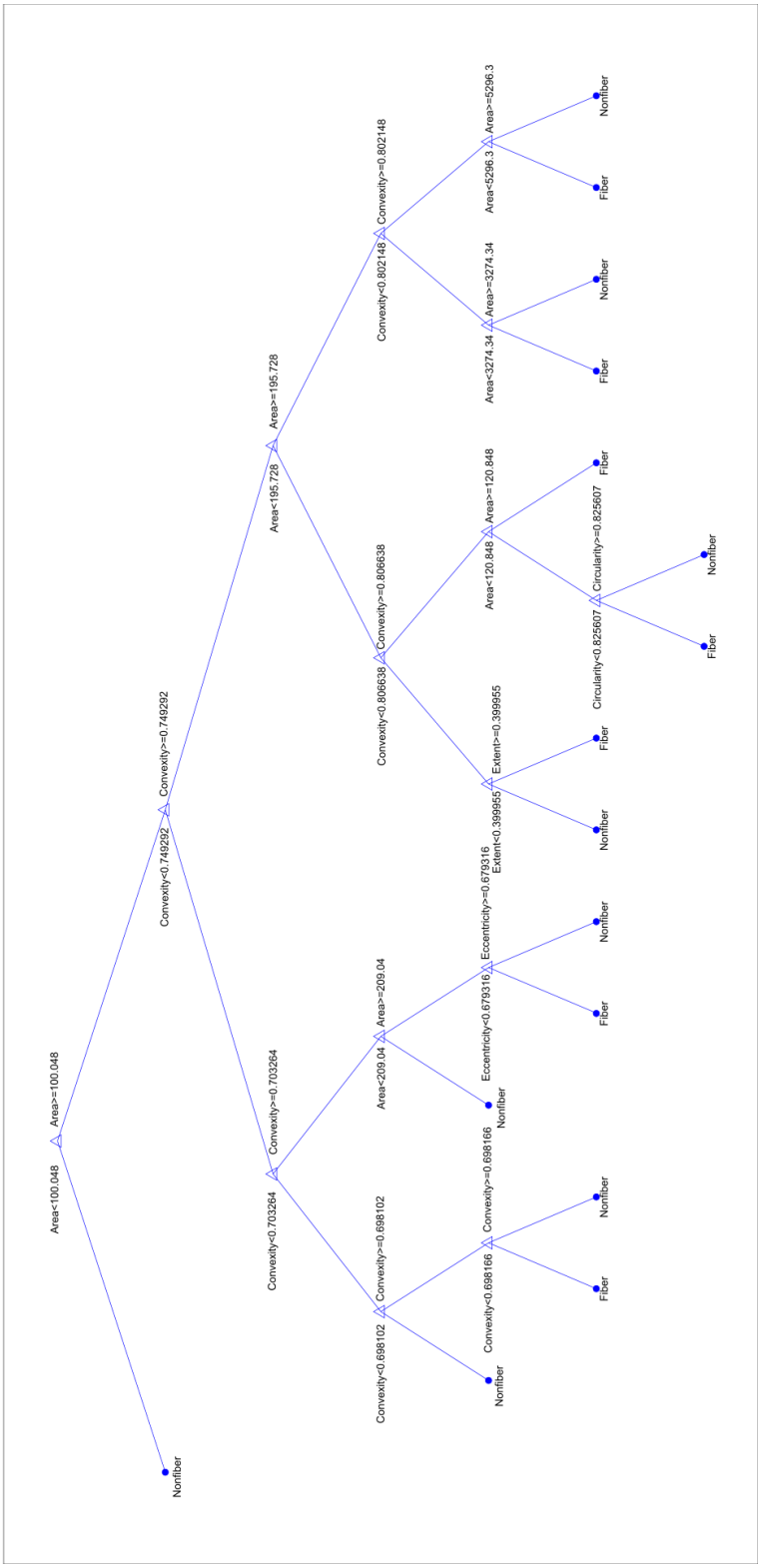

Figure 6. Schematic of the decision tree classifier used in the muscle fiber prediction function. The predictor values for each segment are compared against the values at each branch point until and endpoint is reached, and a classification is assigned.

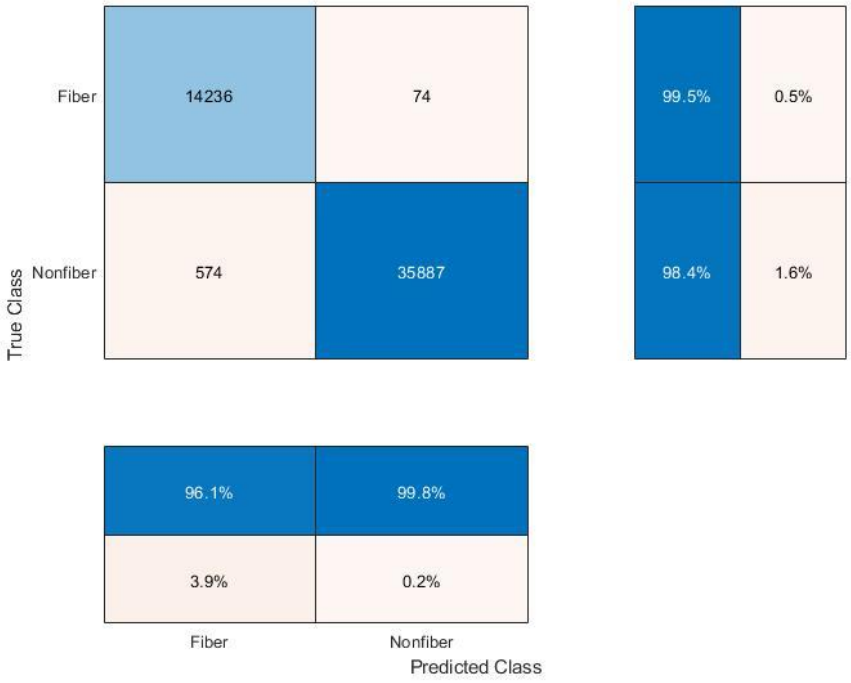

Figure 7. Confusion matrix showing the results of model performance testing. Model predictions on a validation dataset resulted in a true positive rate of 99.5% and a true negative rate of 98.4%.

Data output validation

After a mask containing only muscle fibers is generated, data about the muscle fibers can be output. This includes the number of muscle fibers in the image, the size distribution of the muscle fibers, the type of muscle fiber type, and the position of the nucleus. To assess the performance of SMASH, a series of test images were analyzed manually, using SMASH, and using Myosight, a recently published muscle analysis tool for ImageJ [9]. No significant differences in muscle fiber number were observed between images analyzed with SMASH compared to manual analysis or to Myosight analysis (Fig. 9A). The mean cross-sectional area of muscle fibers measured with SMASH was not significantly different from manual analysis, but

the same fibers analyzed with Myosight were measured to be significantly smaller than both SMASH and manual analysis (Fig. 9B). Similarly, the minimum Feret diameter of muscle fibers was not significantly different between fibers analyzed with SMASH and fibers analyzed manually, but the same fibers were measured to have a significantly smaller minimum Feret diameter when analyzed with Myosight (Fig. 9C).

SMASH is also capable of analyzing specific fiber types if a muscle fiber specific stain is present. Additionally, SMASH can determine whether muscle fibers are centrally nucleated if a

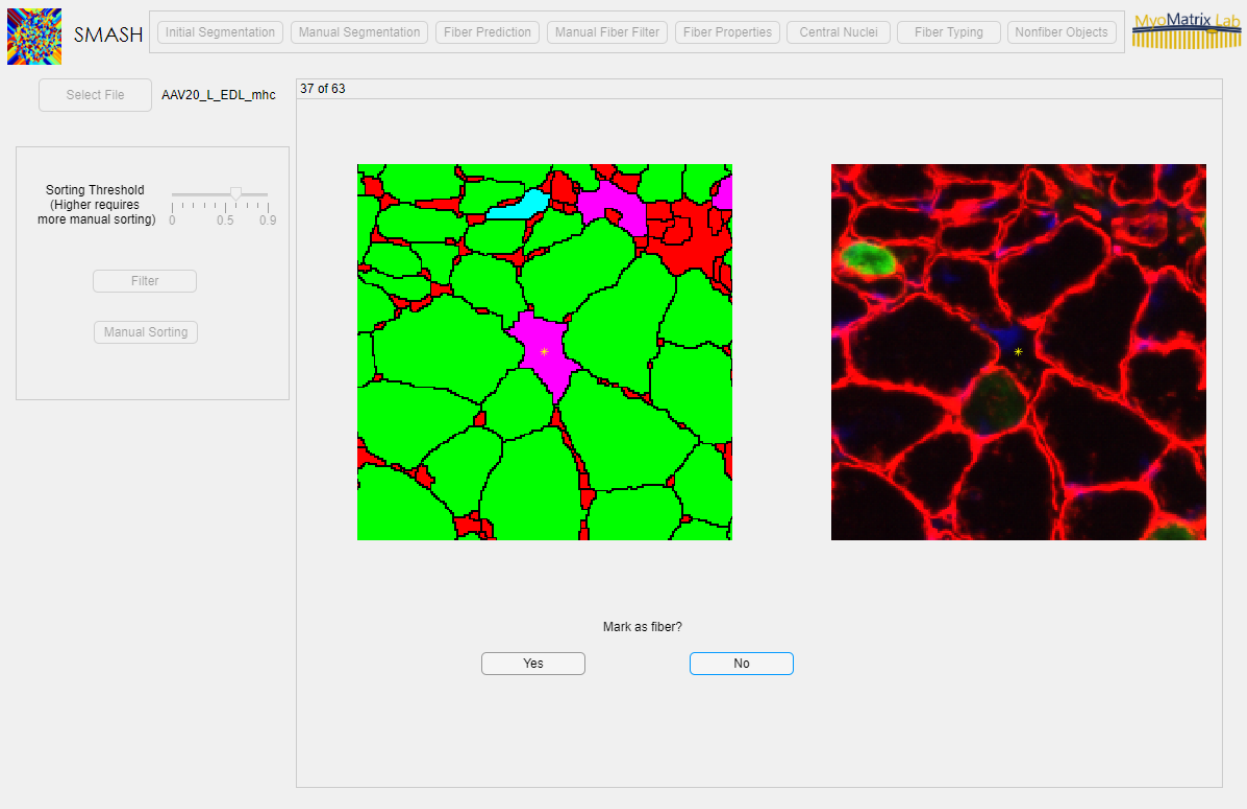

Figure 8. SMASH manual sorting user interface. The left image shows the segments color-coded by prediction. Green indicates a segment is predicted as a fiber and is above the specified threshold. Red is predicted as a nonfiber above the threshold. Magenta and cyan indicate segments predicted as nonfiber and fiber, respectively, that are below the threshold. The right image shows the original image with the segment in question marked with an asterisk.

nuclei stain is present in the image. To validate the performance of these functions, a series of test images were analyzed using the fiber typing and central nuclei function in SMASH as well

as in Myosight. There was not a significant difference in the number of MHC2Bb positive fibers detected by SMASH and Myosight, but the mean cross-sectional area of those fibers was significantly smaller when measured with Myosight compared to SMASH (Fig. 10A, B). The fraction of centrally nucleated muscle fibers was not significantly different when measured with SMASH or Myosight (Fig. 10C).

Discussion

SMASH 2.0 is a complete software package that enables more rapid analysis of muscle cross section images. By passing the image segmentation and fiber prediction steps to machine learning algorithms, less user input is required to achieve robust muscle fiber detection with minimal user bias. The detection is also more consistent and repeatable than manual analysis. The data output by SMASH, including number and cross-sectional area of muscle fibers, number

and cross-sectional area of specific muscle fiber types, and central nucleation, is consistent with manual analysis as well as with other available muscle analysis tools.

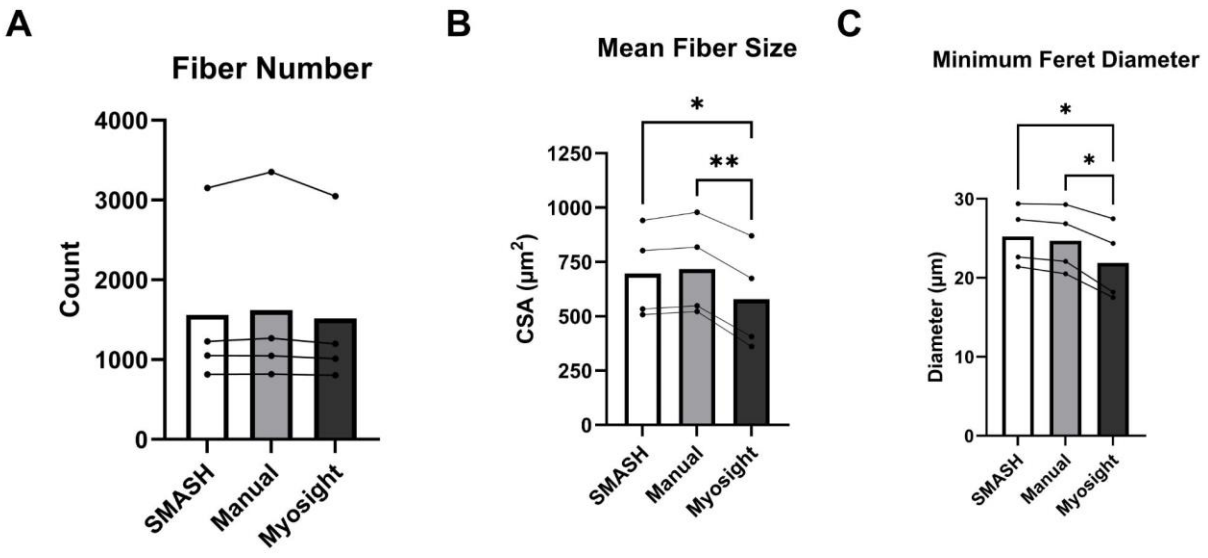

Figure 9. SMASH output validation. (A) number of muscle fibers detected in images was not significantly different between SMASH and other methods. (B) The mean cross-sectional area of muscle fibers measured with SMASH was not significantly different from measurements made manually but was significantly different from measurements made with Myosight. (C) Minimum Feret diameter measurements made with SMASH were not significantly different from measurements made manually but were significantly different from measurements made with Myosight. * $p < 0.05$, ** $p < 0.01$

SMASH only differed significantly from Myosight in muscle fiber area measurements which are likely due to differences in image segmentation methods. Myosight uses a thresholding approach which detects the muscle fibers as the inner edge of the fiber outline stain while SMASH uses the watershed transform and detects muscle fibers as the center of the fiber outline stain. Both approaches work well for the task, but results output by Myosight could be confounded by the brightness of the input images and the number of saturated pixels in the fiber outlines. Using watershed segmentation would avoid this and could lead to more consistent and reproducible results. On the other hand, SMASH and the watershed transform might underperform in cases

where the endomysium that surrounds individual muscle fibers is exceptionally thick. In these cases, muscle fiber size would be overestimated.

Currently, SMASH uses segmentation methods that rely on the contrast afforded by fluorescence and as a result, only immunofluorescent images in TIFF format are compatible with SMASH. Further improvements are necessary to make SMASH compatible with other image formats and stacks as well as with muscle images stained with other non-fluorescent histology stains. Additionally, the machine learning classifiers that SMASH uses were trained exclusively using

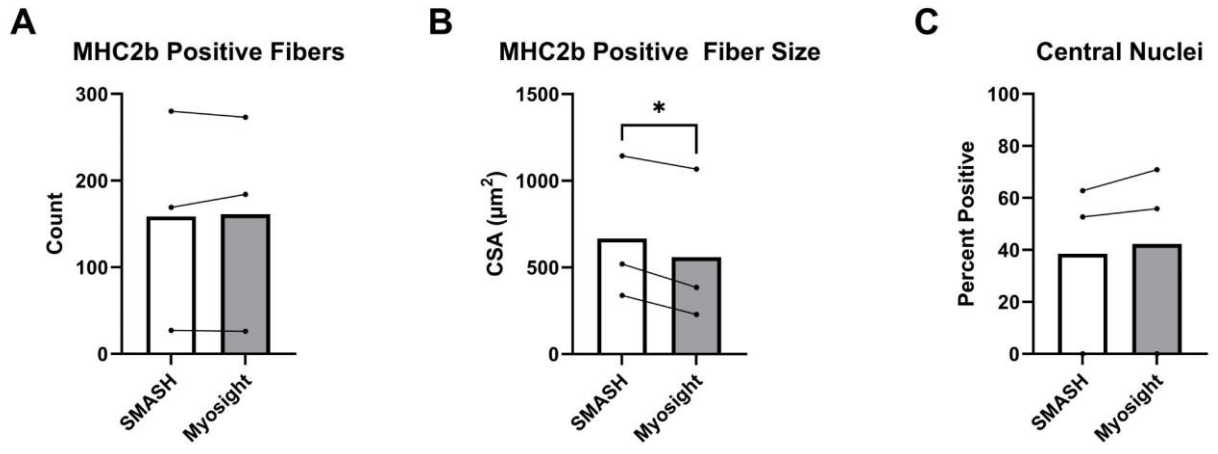

Figure 10. SMASH function validation. (A) The number of MHC2b positive myofibers detected by SMASH did not differ significantly from the number detected by Myosight. (B) The cross-sectional area of MHC2b myofibers was significantly larger when measured with SMASH compared to Myosight. (C) The percentage of centrally nucleated myofibers detected did not differ significantly when measured with SMASH compared to Myosight. * $p < 0.05$

images of mouse muscle. While human muscle fibers have dimensions similar to mice, generating a decision tree for human muscle would likely be required for optimal results. Overall, SMASH 2.0 presents a convenient software package for automatic analysis of muscle histology images and provides outputs including muscle fiber number, cross sectional area, fiber type, nuclei positioning, and nonfiber objects including capillaries and muscle stem cells. The incorporation of machine learning algorithms allows for robust automation with the potential for

the classifiers to evolve as more training data becomes available. With better model training, SMASH could distinguish muscle fibers with greater confidence, particularly in disease states where muscle morphology is more irregular.

Chapter 3. Constricted Migration

Introduction

Skeletal muscle tissue is highly dynamic and is able to undergo robust regeneration of damaged muscle fibers following injury. This repair process is mediated by satellite cells, a population of stem cells that exist at the periphery of muscle fibers beneath the basal lamina, but outside the sarcolemma. Upon damage to a muscle fiber, satellite cells become activated and emerge from the basal lamina before migrating along the muscle fiber to the site of damage where the cells differentiate down a myogenic lineage and fuse with the damaged muscle fiber [1]. During the migration process, the satellite cells encounter the extracellular matrix surrounding individual muscle fibers, termed the endomysium, which is largely composed of type I and type III collagen fibers. Cross linking between collagen fibers can create a porous network that constricts the satellite cells as they migrate through [15]. This leads to impeded cell motility and constriction of the cell's nucleus.

Fibrosis is a pathological buildup of ECM in the muscle following injury and is a hallmark of muscular dystrophy in which the muscles continually undergo cycles of damage and regeneration [4]. The increased density and cross-linking of collagen fibers in fibrotic ECM create smaller pores through which satellite cells must migrate during regeneration. Fibrotic muscles also show an impaired ability to regenerate efficiently and myoblasts from dystrophic patients and animal models have been shown to have excessive DNA damage [16]. We have previously shown that

myoblasts migrated through small transwell membrane pores, but not larger pores, show impaired differentiation and fusion into myotubes [17]. The nuclei of these cells also show nuclear blebbing and DNA damage providing a potential link between constricted myoblast migration, DNA damage, and impaired differentiation.

The transwell assay, however, does not allow for real-time imaging of cell migration through the pores. Microfluidic devices are well suited for this purpose as the direction of cell migration can be shifted to a single focal plane. Microfluidic channel geometry can also be designed to create constrictions of a defined size. PDMS is also suitable for extended live-cell imaging experiments due to its gas permeability and optical clarity. Here we present two microfluidic devices for live cell imaging of constricted myoblast migration, one with channels of a defined size and one which facilitates migration through a tunable collagen matrix.

Methods

Microfluidic Device Design

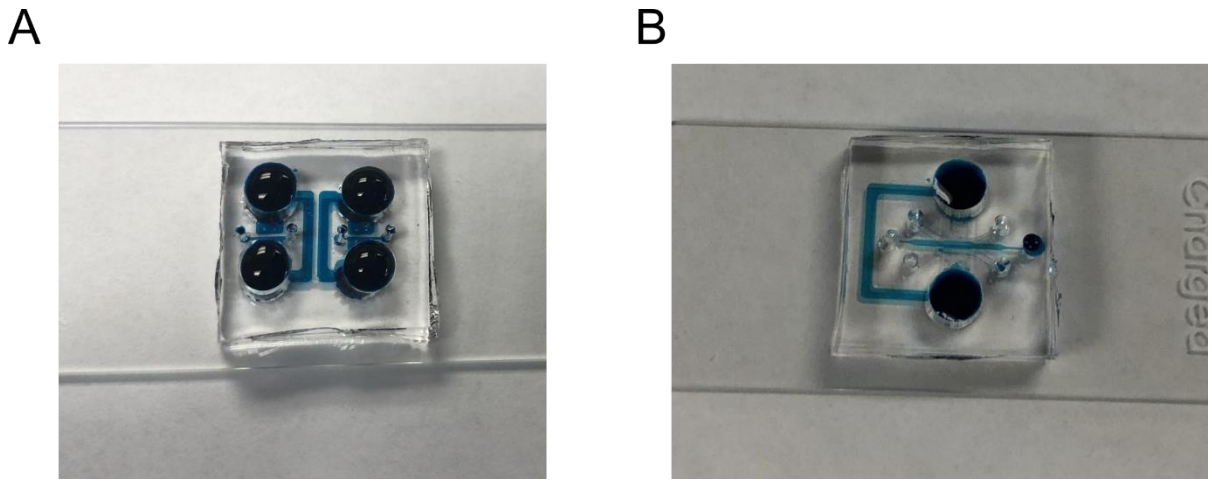

Figure 11. Images of the microfluidic devices. (A) Constricted migration device. (B) ECM device. Blue dye used to visualize channels.

All devices were designed using Autodesk AutoCAD software. The constricted migration device was designed as a modification of a previously described device [18]. The device consists of a series of posts that create several constriction channels in parallel with three sets of constriction channels in series. The spacing between these posts was set to 1.4 μm and 10 μm. These channel widths combined with a channel height of 5 μm create a cross-sectional area identical to the 3 μm and 8 μm diameter transwell membrane pores used previously [17]. The device contains two regions on either side of the constriction area with a channel height of 250 μm for cell culture media and cell loading.

The ECM device was designed using elements of a previously described device, notably, the inclusion of two parallel rows of trapezoidal posts flanking the central channel [19]. These posts were designed to contain a collagen solution within the channel while allowing cells to penetrate the gel once the solution has polymerized or to allow for observation of cells suspended within the collagen gel and the use of chemoattractants on one or both sides of the gel.

Microfluidic Device Fabrication

Microfluidic device molds were fabricated using standard photolithography techniques in the UC Davis Center for Nano-Micro Manufacturing (CNM2) cleanroom facilities. 100 mm-diameter silicon wafers (University Wafer, MA, USA) were dehydrated at 200°C for 15 minutes. SUEX dry film resist (DJ Microlaminates, MA, USA) with a thickness of 250 μm was applied to wafers using a Sky 335R6 laminator. Wafers were aligned with a soda lime photomask (HTA Enterprises, CA, USA) on an EVG620 contact photomask aligner (EV Group, AZ, USA). Wafers were exposed with a UV dose of 1,500 mJ/cm^2 followed by a post exposure bake at 85°C for 40 minutes. Wafers were developed using SU-8 developer (Kayaku Advanced Materials,

MA, USA) for 75 minutes. Wafers were hard baked at 150°C for 30 minutes. The constricted migration device mold was fabricated by Ravata Solutions as a two layer process. The first layer containing the posts forming the migration channels was etched into a silicon wafer to a depth of 5 μm. The second layer containing the cell inlets, media reservoirs and bypass channel was fabricated with 250 μm SUEX as described above.

Microfluidic chips were fabricated via polydimethylsiloxane (PDMS) soft lithography. Sylgard 184 (Dow Corning, MI, USA) monomer was mixed with curing agent at a 10 to 1 ratio by mass and placed in a vacuum desiccator to remove air bubbles introduced during mixing. The PDMS was cast over the silicon molds and placed on a hotplate to cure at 100°C for 1 hour then allowed to cool to room temperature. The cured PDMS was removed from the mold then cut into individual chips and holes were punched for cell seeding ports using a 1 mm biopsy punch while media reservoirs were cut using a 5 mm biopsy punch. PDMS chips and glass slides were treated with oxygen plasma for 90 seconds at a power of 18 W using a plasma cleaner (Harrick Plasma, NY, USA) then bonded to each other. Chips were placed on a hot plate at 90°C for 1 hour to improve bonding strength.

Cell Culture

All experiments were performed using immortalized human myoblasts isolated from muscle biopsies originating from healthy donors [20]. Cells were cultured in a growth medium containing Medium 199 and DMEM in a 1 to 4 ratio supplemented with 20% fetal bovine serum, 25 μg/mL fetuin, 5 ng/ml human epidermal growth factor, 0.5 ng/mL basic fibroblast growth factor, 5 μg/mL insulin, 0.2 μg/mL dexamethasone, and 1% penicillin/streptomycin. Cells were

maintained at 37°C and 5% carbon dioxide. Cells were made to express either tdTomato or 53BP1-mCherry by lentiviral transduction [25].

Microfluidic Device Imaging

Microfluidic devices were imaged using a Leica DMI8 microscope fitted with a CO_2 incubation system at 37° C and 5% CO_2. Devices were imaged for a total of 16 hours with a frame captured every 10 minutes using either a 20x or 40x objective lens.

Results

Constricted Migration Device

To investigate migration through defined constrictions a device was developed with channel geometry similar to the transwell membrane pores used previously. To validate the functionality of the constricted migration device, the inner surfaces of the device channels were functionalized with collagen solution at a concentration of 50 µg per mL. 30,000 human skeletal myoblasts constitutively expressing tdTomato were seeded on one side of the device with 200 µL of cell

culture media. Devices were imaged every 15 minutes for a total of 16 hours and maintained at 37°C and 5% CO_2 for the duration of the experiment.

Devices were also validated with human myoblasts transfected with mCherry conjugated 53BP1, a protein that promotes nonhomologous end joining following double stranded DNA breaks. These cells normally show weak nuclear fluorescence and display bright foci when 53BP1 is

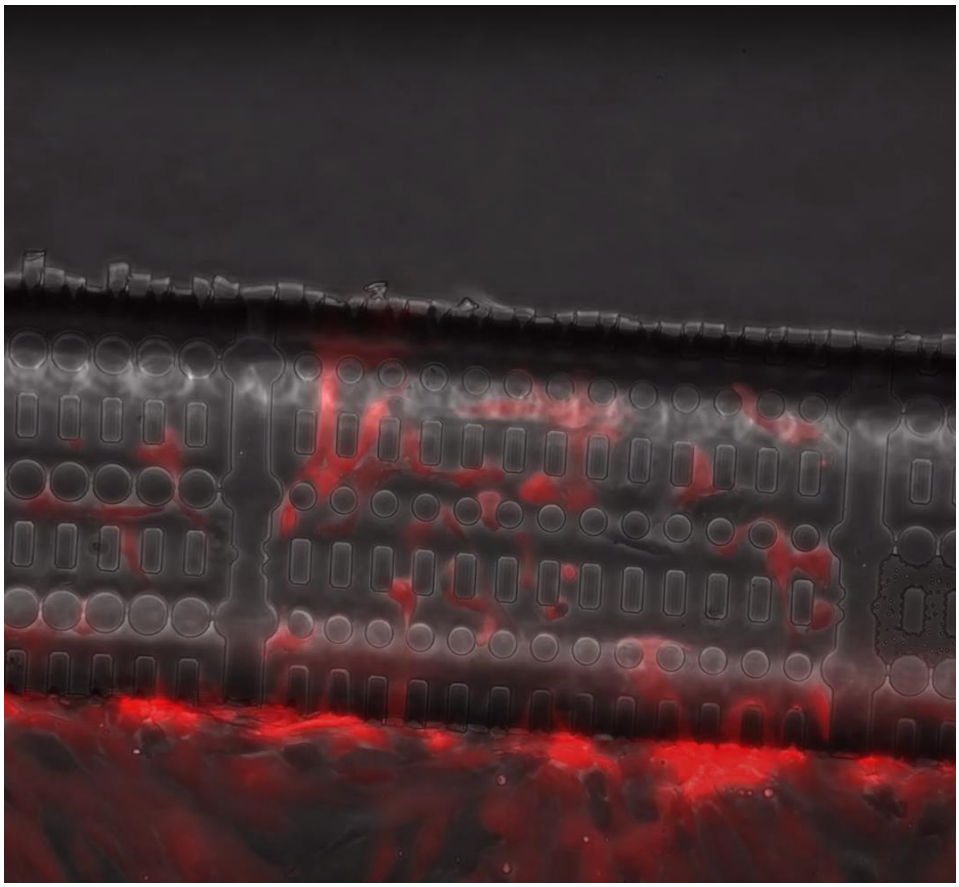

Figure 12. Cells migrate through constriction device channels spontaneously. Human myoblasts expressing tdTomato were observed to migrate through both the 10 μm and 1.4 μm width channels without the use of a chemoattractant.

recruited to the site of DNA breaks. In this way, these cells function as a reporter of DNA damage following constricted migration [25]. Human 53BP1 myoblasts were suspended in myoblast growth medium with fetal bovine serum concentration reduced to 10% at a concentration of 5 million cells per mL. A total of 30,000 cells were seeded into constricted

migration devices and 200 μL of normal myoblast growth medium containing 20% fetal bovine serum was placed in the opposite media reservoir to generate a chemotactic gradient. Cells were observed to migrate through constriction channels toward the high serum medium.

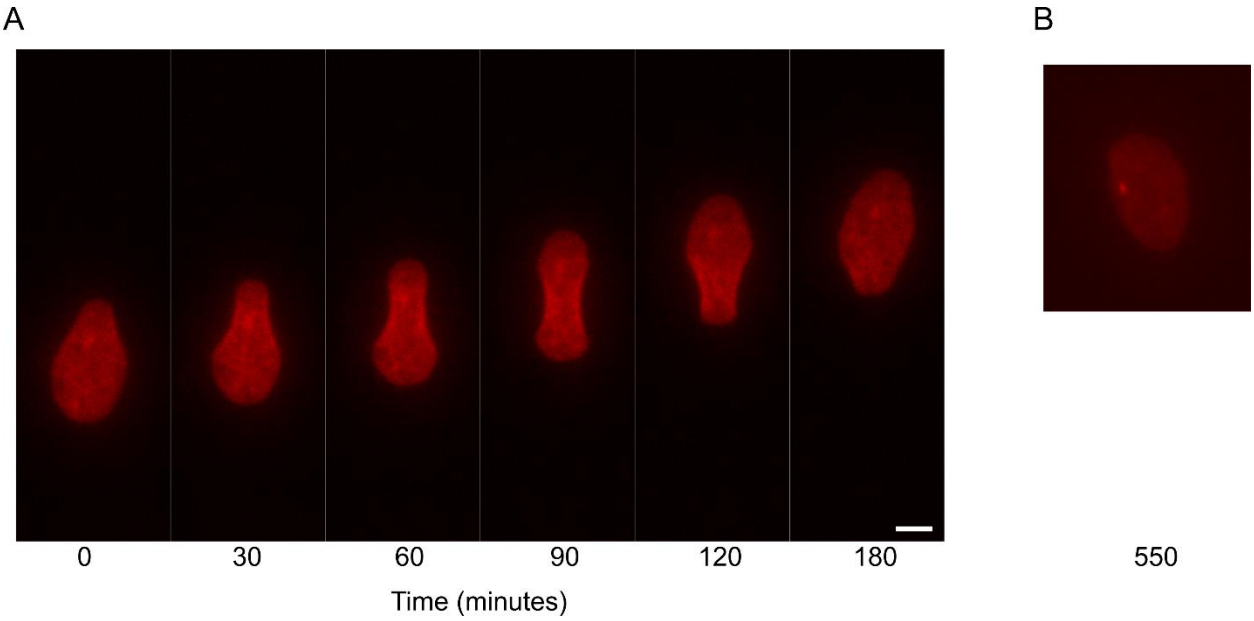

Figure 13. Constricted migration induces double stranded DNA breaks. (A) The nucleus of a 53BP1-mCherry expressing myoblast passing through a constriction during cell migration through the device. (B) The same nucleus showing a bright focus, indicating DNA damage. Scale bar 10 um

ECM Device

To investigate the migration through native ECM substrates a device was designed to accommodate polymerization of a collagen gel while allowing cells access to migrate through. To validate the design of the ECM device, fluid flow through the central channel was simulated with ANSYS Fluent software before fabrication of a silicon master. Fluid density and viscosity were assumed to be 1 g/mL and 1 centipoise, respectively, and flow velocity was set at 0.25 m/sec. Simulation results showed that the fluid was retained within the channel with a minimal amount of fluid escaping between the posts (Fig. 14).

Following fabrication of the ECM device master mold using a similar process as the constricted migration device, devices were fabricated using PDMS soft lithography and devices were tested for their ability to contain a collagen solution as simulated and to polymerize the collagen within the device. A 4.5 mg/mL concentration bovine collagen solution was slowly flowed through the central channel. The solution was retained within the channel as modelled and remained for several minutes. At this point, the collagen was allowed to polymerize at 37°C for two hours. After this time, fibrillar structures indicative of a polymerized collagen gel were apparent (Fig. 15). An initial test of the device was performed by seeding 30,000 human 53BP1-mCherry myoblasts onto one side of the polymerized collagen gel and allowing the cells to migrate through the gel. High serum growth medium was used as a chemoattractant in the reservoir opposite the port the cells were seeded into. Cells were observed to migrate in the device, however, they appeared to migrate under the gel rather than through it indicating poor adhesion between the collagen and the device.

Discussion

Following modification of constricted migration microfluidic device design and fabrication of master molds, devices were successfully validated using tdTomato transfected human skeletal myoblasts. Cells were observed to migrate through both the 1.4 μm and 10 μm diameter constrictions spontaneously without any chemoattractant present (Fig. 12). Cells also remained viable for the full duration of the experiments indicating that devices may be imaged for longer periods of time. Cells expressing fluorescent 53BP1 also showed robust migration through constriction channels. Figure 13 shows one example of a cell nucleus undergoing constricted migration over a period of 180 minutes from the first point that the nucleus appears constricted to

when the nucleus exits the channel. The same nucleus shows a bright focus 550 minutes after the nucleus first entered the constriction indicating the presence of a double stranded DNA break following constricted migration.

The 53BP1 myoblasts are just one possible reporter of nuclear damage. Other reporters that may be used include NLS-tagged fluorescent proteins which allow visualization of nuclear contents

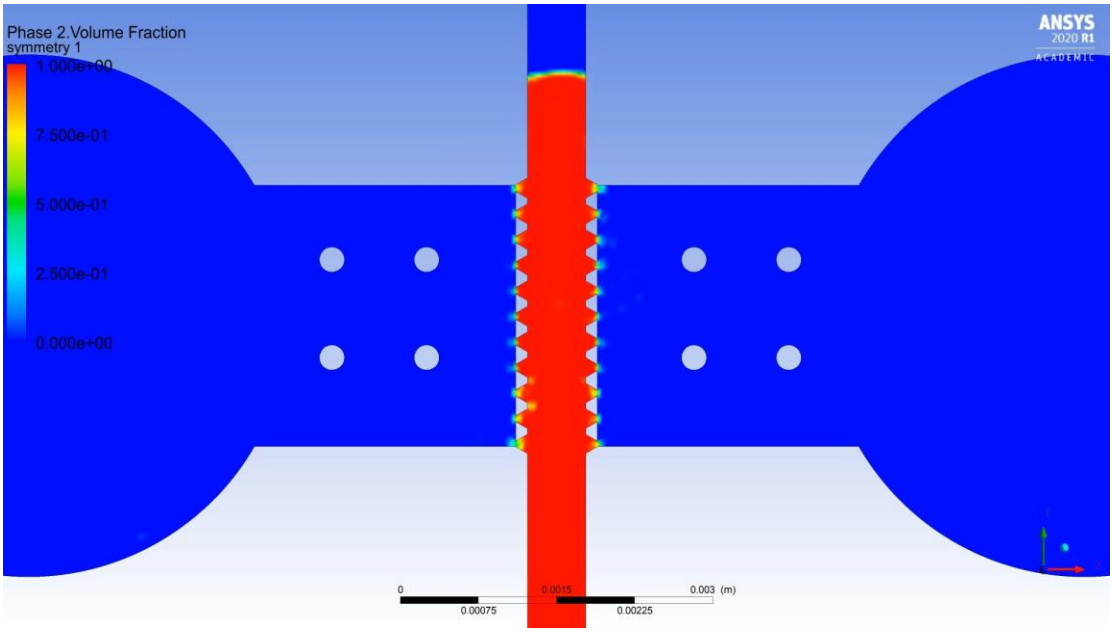

Figure 14. Computational fluid dynamics simulation shows the ECM device can retain collagen solution within the confines of the central channel. Colors represent a volume fraction of fluid where red is the collagen solution and blue is air.

[21]. Loss of nuclear integrity is easily visualized as a leakage of fluorescent protein from the nucleus into the cytosol. Upon entry of DNA into the cytoplasm, cyclic GMP-AMP synthase (cGAS) is recruited to the site where it acts as a cytosolic DNA sensor [21]. Fluorescently labelled cGAS can be used as a reporter of chromatin protrusion into the cytosol following nuclear rupture.

The ECM gel device design was also designed and validated successfully with computational modeling. Devices also performed as modeled and were able to contain a collagen solution within the confines of the central channel with the solution able to polymerize within 2 hours.

Cells seeded into devices with a polymerized collagen gel were viable for at least 24 hours indicating that the devices are suitable for long duration time lapse experiments. The collagen gel showed poor adhesion to the device channel. Optimization of the device will require treatment of glass and PDMS to improve adhesion of collagen gels to the device. We have previously used a treatment of 2% aminopropyltriethoxysilane followed by 0.1% glutaraldehyde for adhering collagen to glass [22] and others have shown that a similar process is also suitable for PDMS [23,24].

Future work consists of a larger scale study using both devices to elucidate the link between constricted myoblast migration and poor myogenic differentiation. The constricted migration device is well optimized to visualize constricted migration through constrictions of a defined size while the ECM device allows for visualization of genetically labeled myoblast migration through pores formed by a more physiologically relevant matrix. Collagen gel pore size can be modulated through changes in collagen concentration, polymerization temperature, and alignment.

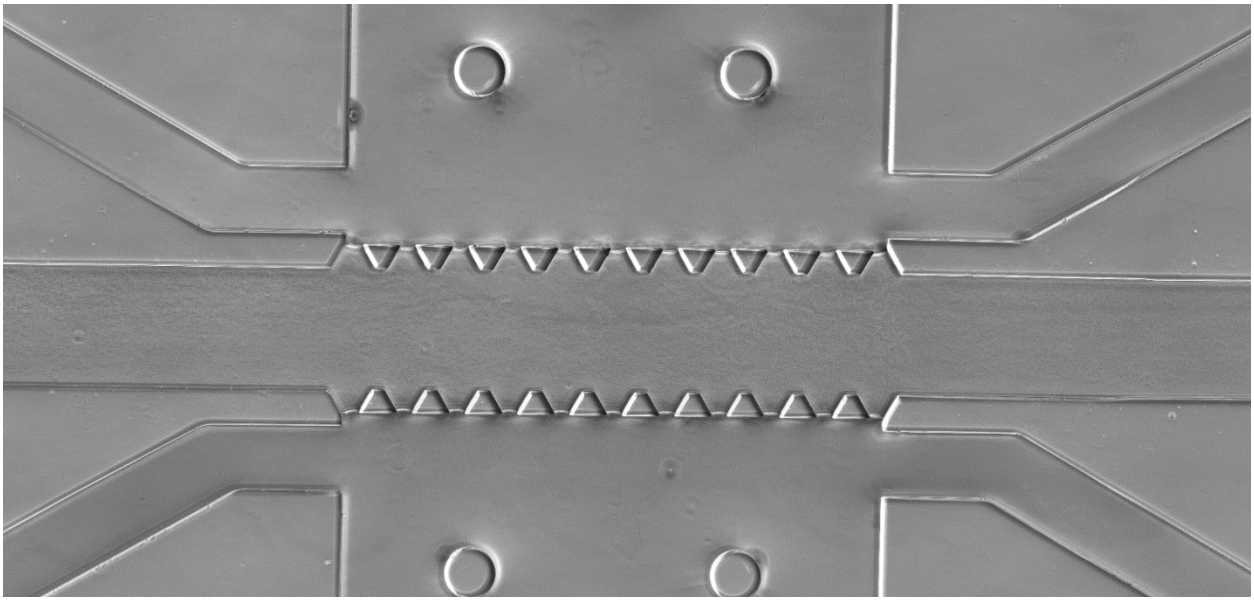

Figure 15. Collagen gel can polymerize in ECM microfluidic device. Microscopic image of the ECM device with fibrillar structure indicative of a polymerized collagen gel retained within the central channel. Scale bar 200 um.

Chapter 4. Conclusions

In this thesis, we present several tools for muscle analysis at the whole muscle and single cell levels. SMASH allows for rapid, automated analysis of immunofluorescent muscle cross sections. The inclusion of machine learning classifiers produces results comparable to manual measurements. SMASH also incorporates multiple functions into one user-friendly app eliminating the need for multiple pieces of software to obtain data about fiber type, myonuclei positioning, and nonfiber objects separately. Ultimately, SMASH will allow the muscle research community to conduct research more efficiently.

The two microfluidic devices allow for observation of the entire myoblast migration process and will help elucidate a causal link between constricted migration and impaired myogenic differentiation. Future large-scale studies can include different readouts for DNA damage and different cell types to recapitulate the heterogeneity of skeletal muscle tissue.

In addition, these tools could have applications in evaluation of therapies for DMD. SMASH can be used to evaluate morphological changes in the muscle in response to therapeutic treatment. Specifically, whether a treatment is able to prevent muscle fiber atrophy or reduce the prevalence of centrally nucleated muscle fibers that are characteristic of DMD. The microfluidic devices allow for single cell assessment of the efficacy of therapeutics that seek to prevent nuclear rupture or to protect satellite cells from the DNA damage that results from constricted migration. In short, these tools can allow researchers to conduct more informed research and develop more effective antifibrotic therapies.

References

1. Yin H, Price F, Rudnicki MA. Satellite cells and the muscle stem cell niche. Physiol Rev. 2013;93(1):23-67.
2. Mahdy MAA. Skeletal muscle fibrosis: an overview. Cell Tissue Res. 2019;375(3):575-588.
3. Schiaffino S, Gorza L, Sartore S, et al. Three myosin heavy chain isoforms in type 2 skeletal muscle fibres. J Muscle Res Cell Motil. 1989;10(3):197-205.
4. Stedman HH, Sweeney HL, Shrager JB, et al. The mdx mouse diaphragm reproduces the degenerative changes of Duchenne muscular dystrophy. Nature. 1991;352(6335):536-539.
5. Chang NC, Chevalier FP, Rudnicki MA. Satellite Cells in Muscular Dystrophy - Lost in Polarity. Trends Mol Med. 2016;22(6):479-496.
6. Wackerhage H, Schoenfeld BJ, Hamilton DL, Lehti M, Hulmi JJ. Stimuli and sensors that initiate skeletal muscle hypertrophy following resistance exercise. J Appl Physiol (1985). 2019;126(1):30-43.
7. Hortobágyi T, Dempsey L, Fraser D, et al. Changes in muscle strength, muscle fibre size and myofibrillar gene expression after immobilization and retraining in humans. J Physiol. 2000;524 Pt 1(Pt 1):293-304.
8. Schiaffino S, Reggiani C. Fiber types in mammalian skeletal muscles. Physiol Rev. 2011;91(4):1447-1531.
9. Babcock LW, Hanna AD, Agha NH, Hamilton SL. MyoSight-semi-automated image analysis of skeletal muscle cross sections. Skelet Muscle. 2020;10(1):33.

10. Wen Y, Murach KA, Vechetti IJ Jr, et al. MyoVision: software for automated high-content analysis of skeletal muscle immunohistochemistry. J Appl Physiol (1985). 2018;124(1):40-51.
11. Desgeorges T, Liot S, Lyon S, et al. Open-CSAM, a new tool for semi-automated analysis of myofiber cross-sectional area in regenerating adult skeletal muscle. Skelet Muscle. 2019;9(1):2.
12. Pertl C, Eblenkamp M, Pertl A, et al. A new web-based method for automated analysis of muscle histology. BMC Musculoskelet Disord. 2013;14:26.
13. Smith LR, Barton ER. SMASH - semi-automatic muscle analysis using segmentation of histology: a MATLAB application. Skelet Muscle. 2014;4:21.
14. Smith LR, Kok HJ, Zhang B, et al. Matrix Metalloproteinase 13 from Satellite Cells is Required for Efficient Muscle Growth and Regeneration. Cell Physiol Biochem. 2020;54(3):333-353.
15. Smith LR, Hammers DW, Sweeney HL, Barton ER. Increased collagen cross-linking is a signature of dystrophin-deficient muscle. Muscle Nerve. 2016;54(1):71-78.
16. Schmidt WM, Uddin MH, Dysek S, et al. DNA damage, somatic aneuploidy, and malignant sarcoma susceptibility in muscular dystrophies. PLoS Genet. 2011;7(4):e1002042.
17. Smith LR, Irianto J, Xia Y, Pfeifer CR, Discher DE. Constricted migration modulates stem cell differentiation. Mol Biol Cell. 2019;30(16):1985-1999.
18. Davidson PM, Sliz J, Isermann P, Denais C, Lammerding J. Design of a microfluidic device to quantify dynamic intra-nuclear deformation during cell migration through confining environments. Integr Biol (Camb). 2015;7(12):1534-1546.

19. Chen MB, Whisler JA, Fröse J, Yu C, Shin Y, Kamm RD. On-chip human microvasculature assay for visualization and quantification of tumor cell extravasation dynamics. Nat Protoc. 2017;12(5):865-880.
20. Mamchaoui K, Trollet C, Bigot A, et al. Immortalized pathological human myoblasts: towards a universal tool for the study of neuromuscular disorders. Skelet Muscle. 2011;1:34.
21. Denais CM, Gilbert RM, Isermann P, et al. Nuclear envelope rupture and repair during cancer cell migration. Science. 2016;352(6283):353-358.
22. Hu LY, Mileti CJ, Loomis T, et al. Skeletal muscle progenitors are sensitive to collagen architectural features of fibril size and cross linking. Am J Physiol Cell Physiol. 2021;321(2):C330-C342.
23. Qian Z, Ross D, Jia W, Xing Q, Zhao F. Bioactive polydimethylsiloxane surface for optimal human mesenchymal stem cell sheet culture [published correction appears in Bioact Mater. 2020 Dec 05;6(6):1810]. Bioact Mater. 2018;3(2):167-173.
24. Beal JH, Bubendorfer A, Kemmitt T, Hoek I, Mike Arnold W. A rapid, inexpensive surface treatment for enhanced functionality of polydimethylsiloxane microfluidic channels. Biomicrofluidics. 2012;6(3):36503.
25. Gentili M, Lahaye X, Nadalin F, et al. The N-Terminal Domain of cGAS Determines Preferential Association with Centromeric DNA and Innate Immune Activation in the Nucleus [published correction appears in Cell Rep. 2019 Mar 26;26(13):3798]. *Cell Rep*. 2019;26(9):2377-2393.e13.